Version of Record: https://www.sciencedirect.com/science/article/pii/S1359645424000922
Manuscript_14593cc33d9f08113ba6e434d834f9d3

Radiation induced segregation in titanium diboride

Shuguang Wei[1,*], Muhammad Waqas Qureshi[1], Jianqi Xi[2], Jun Young Kim[1], Xing Wang[3], Jingrui Wei[1], Ranran Su[4], Longfei Liu[1], William O. Nachlas[5], John H. Perepezko[1], Hongliang Zhang[6,*], Izabela Szlufarska[1,*]

[1]*Department of Materials Science and Engineering, University of Wisconsin–Madison, WI 53706, United States*

[2]*Department of Nuclear, Plasma & Radiological Engineering, University of Illinois Urbana-Champaign, IL 61801, United States*

[3]*Department of Nuclear Engineering, Pennsylvania State University, PA 16802, United States*

[4]*School of Nuclear Science and Engineering, Shanghai Jiao Tong University, Shanghai 200240, China*

[5]*Department of Geoscience, University of Wisconsin–Madison, WI 53706, United States*

[6]*Institute of Modern Physics, Fudan University, Shanghai 200433, China*

[*]*Corresponding authors:*

swei46@wisc.edu (S. Wei)

hlz@fudan.edu.cn (H. Zhang)

szlufarska@wisc.edu (I. Szlufarska)

Abstract

Radiation-induced segregation (RIS) is one of the most dramatic changes that can

© 2024 published by Elsevier. This manuscript is made available under the Elsevier user license
https://www.elsevier.com/open-access/userlicense/1.0/

occur at grain boundaries (GBs) during irradiation. In ceramics, RIS has been rarely studied and the underlying mechanisms are not well understood. Here, we used a combination of experiments and simulations to demonstrate RIS in TiB_2. Specifically, we found that radiation causes a significant B depletion and a modest Ti enrichment in the GB regions. We demonstrate that B depletion is a result of the formation of B_I-V_{Ti} complex and the migration of B vacancies to the GB, where the B_I represents B interstitial and V_{Ti} represents the Ti vacancy. The Ti enrichment is driven by the differences between the diffusivities of Ti interstitials and vacancies. The distinct RIS mechanisms found in TiB_2 shed new light on the relation between the complex energy landscape and defect evolution in ceramics.

Keywords

Radiation induced segregation, titanium diboride, defect migration, anti-site defects.

1. Introduction

Irradiation of materials generates a large number of point defects, which then evolve through recombination, clustering, or segregation to pre-existing defects, interfaces, and grain boundaries [1–5]. Radiation can also lead to changes in the local composition at and near defect sinks, such as dislocation loops and grain boundaries (GB). This phenomenon is known as radiation induced segregation (RIS) [6–12]. RIS has been widely studied in metallic alloys [6–13], where it is known to be driven by the difference in diffusivities of the alloy elements. RIS has been observed in metal

alloys that form solid solutions, which means that in these materials off-stoichiometry at the defect sinks can be easily accommodated [14,15].

Ceramics on the other hand have more complex energy landscapes, related to the covalent and ionic nature of bonding and the presence of multiple sublattices that often have distinct characters. In addition, many ceramic systems used in nuclear applications, such as Ti-B system or Si-C system form line compounds, resulting in a strong thermodynamic driving force to suppress off-stoichiometry. The presence of RIS in ceramics has been demonstrated only recently. Specifically, Wang *et. al.* [16] reported C segregation to grain boundaries (GBs) in SiC after irradiation with Si and C at 300 °C. It was subsequently shown that RIS in SiC plays an important role because it can suppress GB corrosion [17–19] . The mechanism behind RIS in SiC was shown to be related to the presence of a recombination energy barrier for C Frenkel pairs (FPs), which is larger than the migration energy barriers for C vacancy and interstitial [16]. This mechanism reflects the complex energy landscape for defect kinetics in ceramics, and it is different from the typical mechanisms of RIS in metal alloys. However, it is still unclear whether the specific mechanism observed in SiC is general for other ceramics and how RIS, if present, is related to the details of the underlying defect energy landscape.

Several other works have reported elemental segregation in response to radiation, e.g., in TiN [20] and MAX phases [21]. However, it is important to note that in those cases, the segregation was driven by the formation of Xe bubble precipitates under Xe radiation, and not by the intrinsic features of the defect energy landscape of the host

material. For instance, Tunes *et. al.* [20] reported for TiN that Ti enrichment developed both at GBs and at Xe bubbles. The mechanisms behind this Ti enrichment involved the preferential absorption of vacancies by Xe bubbles, which led to an imbalanced flux of Ti interstitials to GBs and to Xe bubbles. In the aforementioned study of MAX phases [21], Cr segregation was reported in Cr_2AlC MAX phases to be driven by a similar mechanism, i.e., Xe bubble selectively absorbed vacancies, causing excess interstitials to diffuse toward defect sinks such as GBs and Xe bubbles, resulting in chemical segregation [21]. Given that the reported RIS was attributed to selective absorption of vacancies by Xe bubbles during precipitation [20,21], and not due to the intrinsic nature of the crystal lattice and the associated defect energy landscape, the prevalence of RIS in ceramics remains an open question.

The titanium boron system is known to form three line compounds, each with an ultra-high melting point of over 2000 °C [22]. Among these, TiB_2, which has the highest melting point of 3230 °C, is considered to be a promising material for structural and high heat flux/plasma-facing applications [22,23] due to its excellent mechanical properties [24–31], good chemical inertness [24], good thermal conductivity [24,26], and potential for deposition on various substrates [32]. A number of studies on radiation damage in TiB_2 have been reported previously [33–37]. For example, a recent study reported by Bhattacharya *et. al.* [38] provided a comprehensive understanding of radiation-induced defects following neutron irradiation of boron-11 enriched TiB_2 at temperatures of ~220 °C and 620 °C [38]. The results revealed formation of dislocation loops and cavities, as well as anisotropic

swelling that led to micro-cracking. However, local changes in composition near GBs were not investigated.

The existence of RIS in TiB_2 is the main focus of the current study. A schematic view of the atomic structure of TiB_2 is shown in Fig. 1. TiB_2 has a hexagonal structure with boron forming networks of boron rings. Radiation effects in the titanium borides were investigated using a combination of focused ion beam (FIB), transmission electron microscopy (TEM), and scanning TEM (STEM), as well as energy dispersive X-ray spectroscopy (EDS) and wavelength dispersive X-ray spectrometry (WDS). Density function theory (DFT) calculations and rate theory modeling are used to explain the trends observed experimentally.

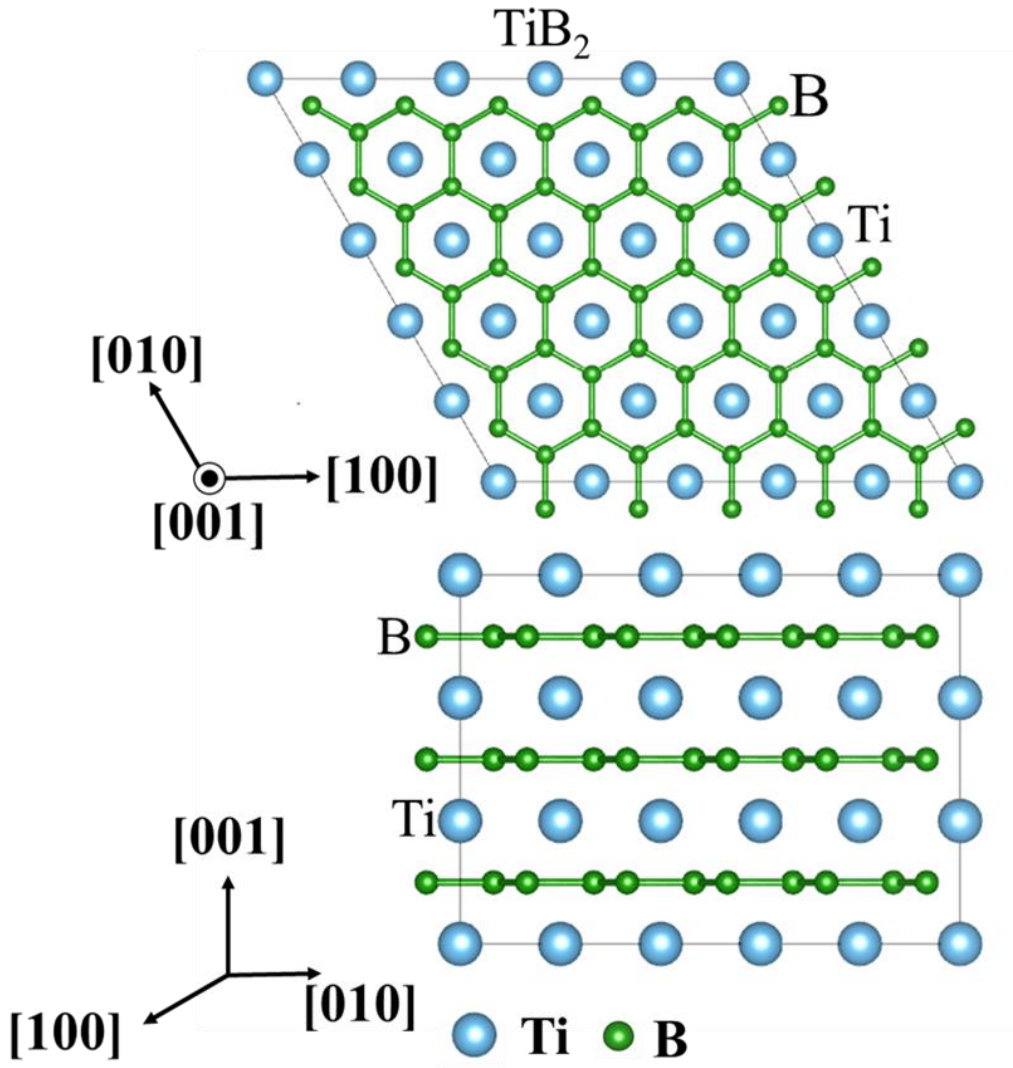

Figure 1. Atomic structure of TiB_2.

2. Methods

2.1. Sample preparation

TiB_2 sample was synthesized using the arc-melting method. TiB_2 powder (99.5 %) was arc-melted in argon and cooled on a water-cooled copper hearth. Polycrystalline TiB_2 sample was later annealed at 600 °C for 6 h to release residual stress. The annealed sample was then cut using a wafering blade and polished using diamond

lapping film discs.

To confirm the elemental distribution of synthesized TiB_2 sample, we performed EDS area scan on TiB_2 using an FEI Helios PFIB G4 equipped with the Thermo Noran Energy dispersive X-ray microanalysis system, operated at 15 kV. Based on the EDS mapping, both Ti and B exhibited uniform distribution in TiB_2. To further confirm the stoichiometry of TiB_2, elemental concentration of polished TiB_2 sample was measured using a Cameca SX-Five field emission electron probe microanalyzer (EPMA) operating at 10 kV accelerating voltage and 4 nA current density. Ti metal (99.995 %) and B metal (99.5 %) were used as calibration standards. Quantification of B concentration in the presence of Ti requires separating B Kα X-rays at 0.183 kV from the interference with Ti Ll (n=2) at 0.198 kV. This was accomplished by using 160 mm diameter spectrometer equipped with LPC2 synthetic multilayered diffraction crystal ($2d$ = 98 Å) and applying differential Pulse Height Analysis (PHA) mode in the *Probe for EPMA* analysis software. Adjustment of PHA conditions on a B standard was performed at 1 nA to avoid pulse height depression which can result in overestimation of B contents [40]. A probe size of ~200 nm was used to acquire measurements along linear traverses with a 3 μm step size. Only those measurement results with analytical totals between 98-102 % were accepted before calculating the normalized atomic ratio. From the measured concentration, the TiB_2 was found to have stoichiometry of 1.00:2.00 for Ti:B. Detailed elemental characterization of TiB_2 is provided in Supplementary Materials (Fig. S1 and Fig. S2).

2.2. Radiation test

To investigate the RIS in TiB_2, an irradiation experiment was conducted using the tandem accelerator at Ion Beam Lab, University of Michigan with a 3.00 MeV silicon ions beam to a total fluence of 1.47×10^{16} ions·cm^{-2} at 600°C. The duration of irradiation was set to be 5 h. Irradiation induced damage in TiB_2, measured in dpa, was simulated using SRIM-2013 [41], and the threshold energies for Ti and B were set to be 25 eV and the Kinchin-Pease damage calculation was used. The damage profile as a function of depth from the top surface is plotted in Fig. 2. The profile exhibits a relatively flat trend in the depth range of 200 nm to 600 nm, which is the damage plateau. The irradiation damage in this plateau was calculated to be 1.0 dpa and then increased to ~6.0 dpa at the depth of ~1200 nm.

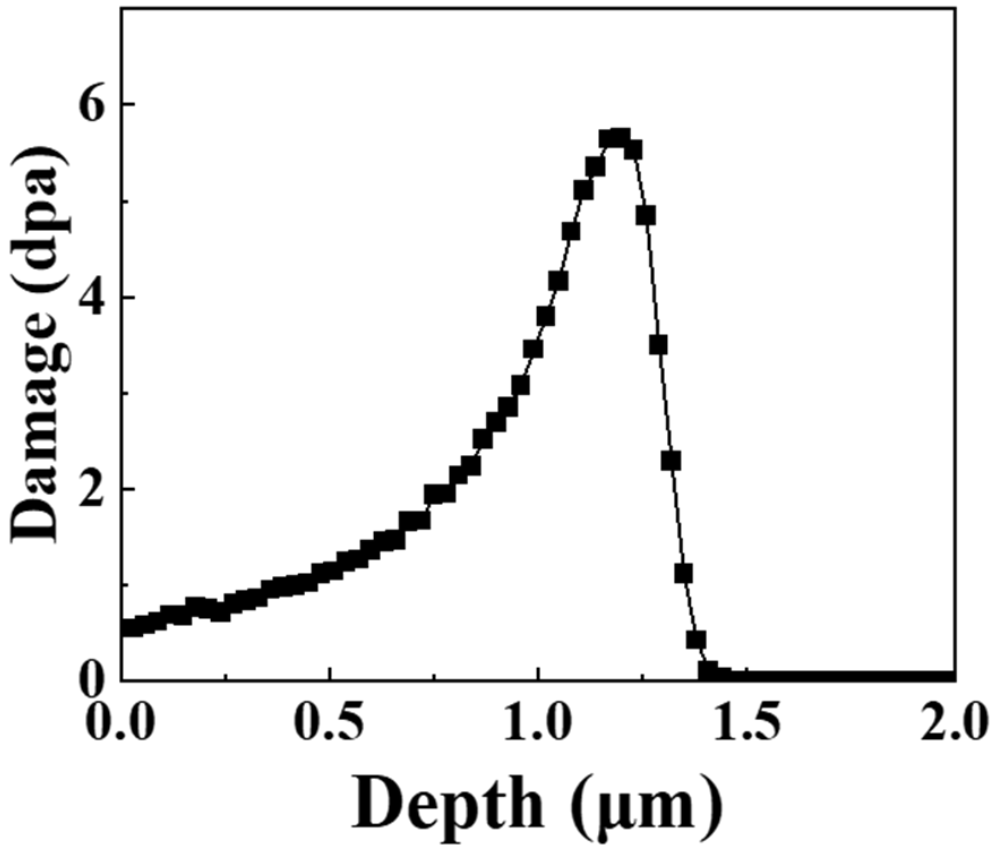

Figure 2. Irradiation damage in dpa versus depth profile for TiB_2 at the fluence of 1.47×10^{16} ions·cm^{-2}.

2.3. Materials Characterization

Electron-transparent samples used in TEM analysis were prepared with a standard lift-out technique using an FEI Helios PFIB G4 FIB/FESEM Focused Ion beam (FIB) in the Nanoscale Imaging and Analysis Center, University of Wisconsin-Madison. Pt protective layers with a thickness of ~6 μm were deposited on the designated areas on the irradiated samples to protect the surface from damage by the FIB ion beam. The protective Pt layers were deposited in two steps. First, Pt layers with the thickness of ~1 μm were deposited using a 5 kV electron beam. Second, Pt layers with the thickness of ~5 μm were deposited on top of electron beam deposited Pt protective layers. After final thinning in FIB with a 30 kV ion beam to a thickness of ~150 nm, the samples were cleaned using a Fischione 1040 TEM Ion Mill with an 800 V ion beam to remove the amorphous layers induced by the ion beam during the sample preparation process. As a reminder, the nano mill or ion mill was used solely for removal of the amorphous layer. The ion mill was applied to both sides of the FIB sample for 15 min, which will not induce significant damage. Furthermore, we have estimated the damage induced by the ion mill using SRIM calculation (Fig. S3). The analysis indicated that the ion milling damaged region with a damage level exceeding 1 dpa was confined to a depth of no more than 2.4 nm, which is much smaller when compared to the thickness of the FIB sample. Consequently, the effects of the ion milling on RIS can be neglected. The misorientation angles of GBs in TiB_2 samples were determined using the transmission electron backscatter diffraction (t-EBSD)

with a tilt angle of 45 ° and a voltage of 25 kV in the Helios PFIB. A representative high angle GB with a misorientation angle of ~ 73° in TiB_2 after irradiation was characterized using STEM and t-EBSD (Fig. 3). We have also employed a comprehensive set of analytical techniques to confirm that the GBs are oriented edge-on. For instance, t-EBSD was used to acquire diffraction pattern from regions in close proximity to the GBs (i.e., <1 nm). We observed distinct Kikuchi patterns in these near-GB areas for both grains, thereby affirming the crystalline nature of the material adjacent to the GBs. Importantly, no overlap was detected in the Kikuchi patterns corresponding to the two grains within the GB regions. This absence of pattern overlap serves as compelling evidence that the grains at the GBs are indeed oriented edge-on, as shown in Fig. 3c. If the GB were not oriented edge-on (Fig. 3d), these Kikuchi patterns would overlap with each other. To further corroborate the edge-on orientation of the GBs, we compared the observed Kikuchi patterns with simulated patterns based on the known crystal structure of the material. The high degree of congruence between the observed and simulated patterns further validated our conclusion regarding the edge-on orientation.

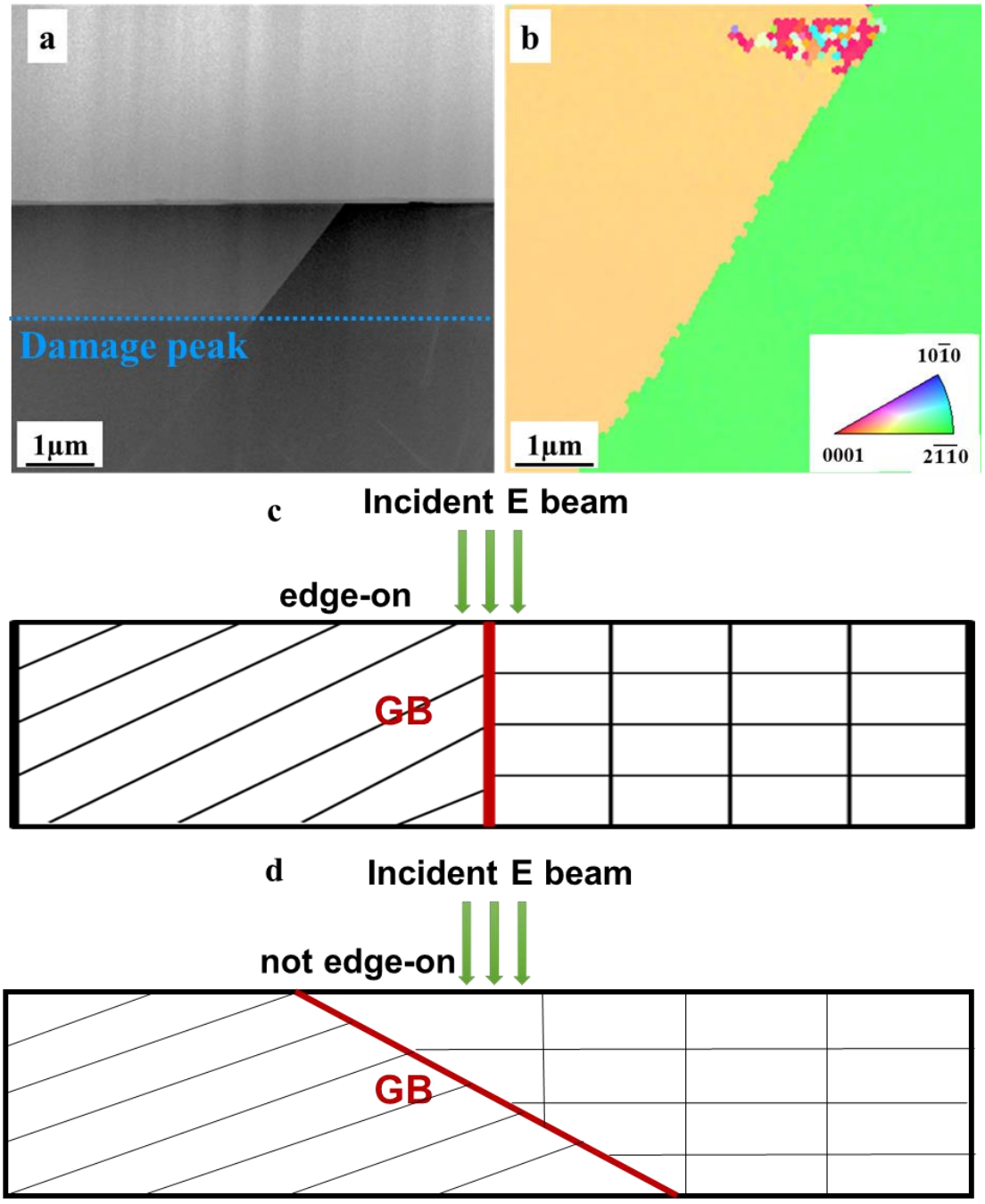

Figure 3. Grain boundary (GB) in TiB_2. (a) STEM image of irradiated GB with a damaged region ranging from the surface up to the depth of 1700 nm and an annealed region beyond 1700 nm. (b) t-EBSD image of the same GB with different colors to distinguish grain orientations. The noise near the top of the image is caused by radiation-induced lattice distortion. The misorientation between the two grains is ~73 °. Schematic illustrations of GB, which is (c) edge-on to the incident electron beam and (d) not edge-on to the incident electron beam.

Chemical analysis near the GB was conducted using high-angle annular

dark-field STEM (HAADF-STEM) images and EDS in an FEI Titan G2 80-200 TEM equipped with the Super-X EDS detection system. The accelerating voltage, probe current and probe convergence angle were set to be 200 kV, ~300 pA, and 23 mrad for the chemical analysis, respectively. To determine whether RIS exists in TiB_2, line scans were performed in at least 4 different regions at the GB both in unirradiated and irradiated samples, and the reported composition profile for each sample corresponds to an average value calculated over at least four line scans. Each line scan was performed with a step size of 0.25 nm, a dwell time of 15 s, and a spot size of 6 to get strong signals and good statistics. Drift correction was conducted using the acquired HAADF images, and a time interval of 60 s between two drift corrections was used. To further validate the prevalence of RIS in TiB_2, point scans were carried out on multiple TiB_2 TEM samples. These point scans encompassed a minimum of 6 distinct positions along the GB and within the grain interior on both sides of the measured GB to obtain average values. Additionally, point scans were conducted in the irradiated and unirradiated regions. For each point scan, a dwell time of 60 s and spot size of 6 were used to enhance peak intensity and improve the signal-to-noise ratio. The B and Ti peaks collected at each scan were later analyzed as follows: (1) Peak Fitting: Gaussian distribution was employed to fit each peak. (2) Area Calculation: The area under the Gaussian distribution curve for each peak was measured. (3) Stoichiometry Validation: The EPMA measurement (Fig. S2) confirmed that our TiB_2 sample is stoichiometric. Therefore, we established a reference Ti peak intensity to B peak intensity ratio in the bulk region (far from the grain boundary). This reference

represents a Ti to B ratio of 1:2 and was determined by averaging the Ti peak to B peak intensity ratios from 12.5nm to 7.5nm form the GB for each line scan or averaging the Ti peak to B peak intensity ratios of all points collected in bulk region (at least 7.5 nm away from the GB) for each set of point scan. (4) Composition Analysis: Subsequently, the Ti peak intensity to B peak intensity ratios for all scans were calculated, and the compositions were determined using the reference average ratio obtained from the bulk region.

2.4 Computational methodology

DFT calculations were performed using the Vienna Ab-initio Simulation Package [42] with the projector augmented wave [43] and the generalized gradient approximation by Perdew, Burke, and Ernzerhof [44]. The plane-wave cutoff energy of 450 eV and Monkhorst-Pack k-point mesh [45] of 12×12×12 (TiB_2) were set with the energy tolerance of 0.1 meV/atoms. The calculated lattice constants for TiB_2 were a = 0.302 nm, c = 0.319 nm (TiB_2), in good agreement with the experimentally determined lattice constants [36].A supercell of 5×5×3 is selected to calculate the total energy of perfect supercell as well as defective supercell based on the results of convergence tests.

To find the most stable defects, we calculated the defect formation energy (E_f),

$$E_f = E_{\mathrm{d}} - E_{\mathrm{p}} + \sum n_i \mu_i \quad (1)$$

where E_d is the total energy of a defective supercell, E_p is the total energy of a perfect supercell, n_i is the number of atoms removed or added when introducing a defect, and μ_i is the chemical potential of the defect element. The μ_i is calculated by using a

similar strategy to that of Kim *et. al.* [46]. The μ_{Ti} and μ_B for Ti-rich and B-rich conditions are tabulated in Table S1. The formation energies of defects are calculated using the chemical potential at the halfway point between the Ti-rich and B-rich environments.

To rationalize RIS in TiB_2, we calculated migration energy barriers of point defects and the energy barriers of Frenkel Pair (FP) recombination, using the climbing image nudged elastic band method [47].

3. Results and discussions

3.1. Observation of RIS in TiB_2

To investigate the existence of RIS in TiB_2, the composition in the vicinity of three high-angle GBs (HAGBs) was characterized using STEM based EDS. All GBs were confirmed to be HAGBs based on STEM HAADF and the t-EBSD images. A representative HAGB is shown in Fig. 3. The misorientation angle and Miller indices of the grains on both sides of each GB were determined using the t-EBSD and it was determined that the misorientation angles of all GBs investigated in this study ranged from 24 ° to 73 °. A summary of the misorientation angles and Miller indices can be found in Table 1 and Table 2. All HAGBs were lifted out from the TiB_2 sample that was irradiated using 3 MeV silicon ions at 600 °C. According to SRIM calculations (Fig. 2), the damage level increased to a peak of ~6.0 dpa and then decreased to 0 dpa at the depth of ~1500 nm. Experimentally, the damage level was found to decrease to zero at the depth of ~1700 nm. Accordingly, the HAGB was divided into two regions: an *irradiated region* that extends from the surface up to the depth of 1700 nm and an

annealed region beyond 1700 nm, where the sample was not damaged by ions, but was annealed during the irradiation with the same temperature profile as the damaged region.

To understand the impact of radiation on the local concentration at GB, it is important to characterize the unirradiated GB. To set the reference, the local concentration at the HAGB with a misorientation angle of 54 ° within the annealed region, which was not affected by the ion damage, was evaluated. The characterization involved conducting a minimum of four EDS line scans at various positions spanning depths of 1900 nm to 3000 nm. The final concentration profile near GB in Fig. 4a was averaged over all the line scans. The error bars were calculated as the standard deviation from the mean. As illustrated in Fig. 4a, the concentration profiles of both B and Ti exhibit some fluctuations. However, the fluctuations are mostly within the error bars of the measurements. In addition, although the concentrations at GB and in the grain interior of the non-irradiated sample (Fig. 4a) are not exactly the same, the differences are relatively small. Specifically, the B concentration at GB was measured to be 65 at.% and Ti concentration at GB was measured to be 35 at.% (Fig. 4a). The B and Ti concentrations measured using EPMA were 66.67 at.% and 33.33 at.%, respectively, which is consistent with the overall stoichiometry. The B concentration of 65 at.% measured in GB is very close to the average B concentration of 66.67 at.%, suggesting that GBs in TiB_2 are near stoichiometric. To corroborate the finding that GBs in TiB_2 are near-stoichiometric, we carried out more EDS measurements at

different GBs in annealed regions (Table 1). Specifically, HAGBs with misorientation angles of 24 ° and 72 ° were characterized and the B concentrations were measured to be 66 at.% and 67 at.%, respectively, which further confirmed the intrinsic near-stoichiometry of GBs in TiB_2.

Table 1 | EDS measurements at annealed regions of three HAGBs

GB No.	B conc. (at. %)	Fab.	T_{anneal} (°C)	Mis. Angle (°)	Miller indices
1	66	FIB	600	24	$(\overline{25}\ 5\ 7)//(19\ 50\ \overline{44})$
2	67	FIB	600	72	$(\overline{45}\ 29\ 50)$ // (9 100 2)
3	65	FIB	600	54	$(3\ \ 11\ \bar{4})$ // (31 27 102)

Using the GB concentrations in the annealed region as a reference, we can now explore the effects of radiation on GB concentration. Similar to the measurements in the annealed region, at least four line scans were conducted at different positions ranging from a depth from 900 nm to 1700 nm within a HAGB with a misorientation angle of 73 ° (Fig. 3) Average concentrations based on all measurements from the different line scans are plotted in Fig. 4b. Comparison of concentration profiles in Fig. 4b to those shown in Fig. 4a reveals clear differences between the annealed (unirradiated) GB and the irradiated GB. In contrast to the relatively flat concentration profiles in the annealed region (Fig. 4a), the concentration profiles in the irradiated region exhibit noticeable radiation induced B depletion in the GB region (Fig. 4b). Specifically, the B concentration near the GB dropped to 61 at.% and a valley of ~4 nm in width could be observed in the vicinity of the GB (Fig. 4b). The existence of

RIS in TiB_2 was further confirmed through two additional measurements on HAGBs with different misorientation angles (Table 2). For example, B concentrations at HAGBs with misorientation angles of 50 ° and 72 ° were measured to be all ~64 at.%, which were lower than those measured in the grain interiors on both sides of the HAGBs. The consistent observation of radiation induced B depletion in all measured HAGBs leads to the conclusion that RIS is indeed present in TiB_2. No evidence of precipitates was found in the TiB_2 based on our STEM analysis. It is worth mentioning that the local composition of the low angle GBs (LAGBs) was not measured in TiB_2. Instead, the focus was on HAGB due to their common occurrence. Thus, whether the RIS also exists in LAGB is still an open question. For instance, Wang *et. al.* [16] studied RIS in SiC and they observed RIS in HAGBs, but not in LAGBs.

Table 2 | EDS measurements at damaged regions of three HAGBs

GB No.	B conc. (at. %)	Fab.	T_{Irr} (°C)	Mis. Angle (°)	Miller indices
1	61	FIB	600	73	$(\overline{91}\ 58\ 100)$// (37 50 15)
2	64	FIB	600	50	(100 3 12) // $(\overline{45}\ 5\ 3)$
3	64	FIB	600	72	$(\overline{45}\ 29\ 50)$ // (9 100 2)

Based on the relative concentrations (Fig. 4b), it is unclear whether the concentration change is caused by B depletion or by Ti enrichment. To address this question, we measured the peak count ratio for both B and Ti. As discussed by Wang *et. al.* [16], the areas below the EDS peaks (peak counts) are proportional to the

atomic density of the elements. Therefore, the peak count ratio can reflect the percentage change in the atomic density of elements near the GB relative to that in the grain interior. The peak count ratio of the annealed region and the irradiated region is calculated and plotted in Fig. 4. In the annealed region, the peak count ratio profile of Ti is flat with negligible fluctuations, suggesting a negligible change in Ti element density near the GB (Fig. 4c). The peak count ratio profile of B is noisier, which is due to the relatively low peak counts of the B peak (Fig. 4c). However, there is still no significant change in the B element density near the GB of the unirradiated sample (Fig. 4c). After irradiation, clear changes in element density can be observed in Fig. 4d, especially when compared with annealed regions in Fig. 4c. Specifically, the Ti peak count ratio is relatively flat with a small increase by ~7 % near the GB (Fig. 4d). In addition, the B peak count ratio drops to 78 % at the GB. As a result, the segregation observed in TiB_2 is attributed to significant B depletion as well as modest Ti enrichment.

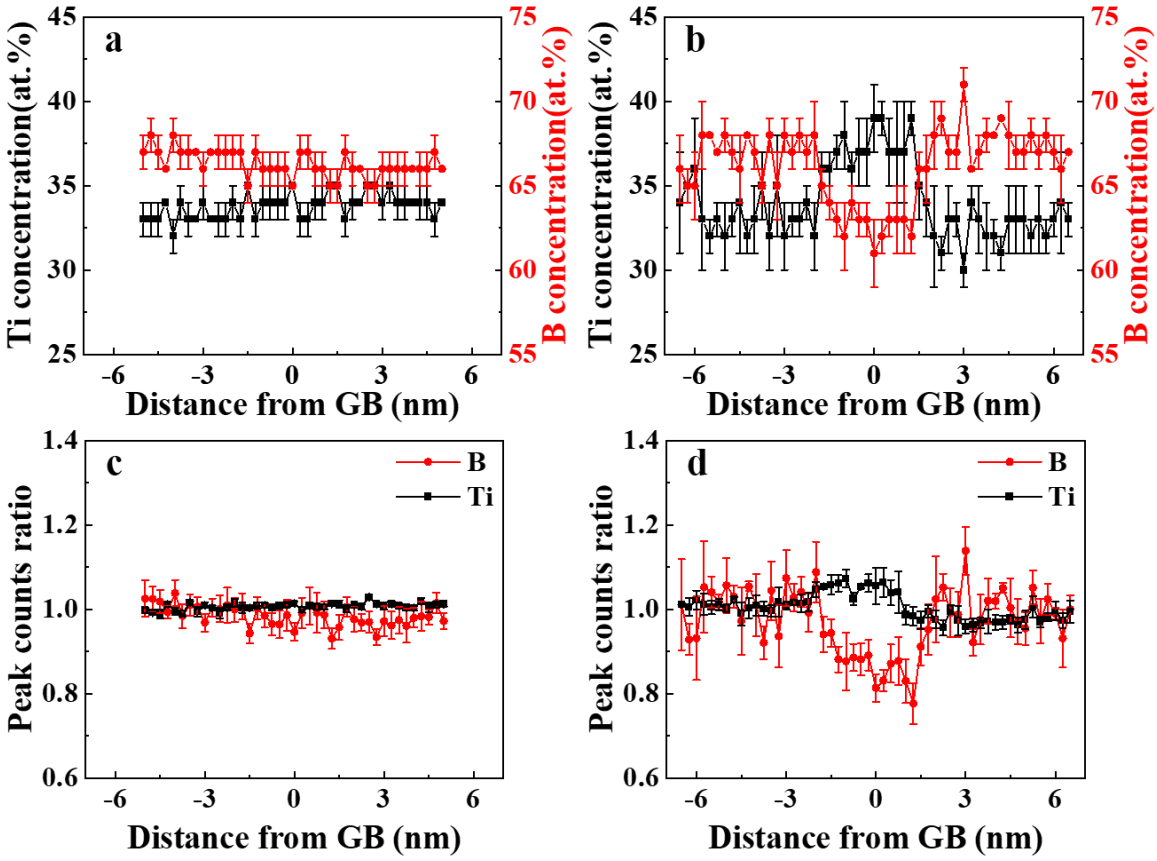

Figure 4. Local elemental compositions in TiB_2 outside the irradiation region (annealed) and irradiated at 600 °C. (a). Relative Ti and B concentration near the GB measured in the annealed region. The concentrations were averaged over 7 measurements at the depth of 1900 nm and 3000 nm from the surface. (b). Relative Ti and B concentration near the GB measured in the damaged (irradiated) region. The concentration was averaged over 4 scans at the depth ranging from 900 nm to 1700 nm. (c). Typical peak count ratios near the annealed (non-irradiated) GB and (d). Typical peak count ratios near the damaged (irradiated) GB. The error bar corresponds to the standard deviation from the mean.

3.2. Mechanisms of RIS in TiB_2

We can exclude the possibility that the segregation in TiB_2 is induced by thermal

annealing. To begin with, segregation due to thermal annealing was mostly reported at a temperature higher than 0.4 T_m, where T_m is the melting temperature [48–51]. For TiB_2, the investigated temperature of 600 °C is only 0.25 T_m as the melting temperature of TiB_2 is 3230 °C. In addition, if the segregation was introduced by the thermally induced defects migration from the grain interior to the GB, then such segregation would be observed along the entire GB, not only in the irradiated region. However, the segregation was solely observed in the irradiated region instead of along the entire GB. Since the main contributor of the segregation is the B depletion, it is also important to ask whether the segregation is induced by B atoms out-diffusion along the GB to the surface, which in principle could also be driven by thermal annealing [52–54]. To answer this question, we estimated the energy barrier for atoms in TiB_2 to diffuse a certain distance l along the GB using the following equation [55],

$$E = -kT\ln(\frac{l^2}{2D_0 t}) \quad (2)$$

Here, E is the migration energy barrier, k is the Boltzmann constant, T is the experimental temperature, which is 600 °C, t is the diffusion time of 5 h, and D_0 is the diffusion pre-factor, which was assumed to be 2.0×10^{-7} m^2/s. However, even if D_0 varies in a relatively large range, i.e., by one to two orders of magnitude, the conclusion drawn in this paragraph is still true. According to Eq. 2, the migration energy barrier depends logarithmically on the diffusion length and this dependence is plotted in Supplementary Materials (Fig. S4). As discussed in Section 3.1, the concentrations at the GB were measured at depth ranging from 900 nm to 1700 nm for the irradiated region and from 1900 nm to 3000 nm for the annealed region. RIS

was observed at the depth of 1700 nm but not at the depth of 1900 nm. Based on equation 2, the migration energy barriers for defects diffusing distances of 1700 nm and 1900 nm were estimated to be 1.63 eV and 1.61 eV, respectively. Though the energy difference of 0.02 eV can stop the diffusion of B atoms from non-damaged GB at a depth of 1900 nm to the surface, it cannot prevent the diffusion of B atoms from a depth of 1900 nm to a depth of 1700 nm along the GB. As a result, one would expect B depletion to be observed at the depth of 1900 nm, albeit potentially to a lesser degree. In contrast, no obvious B concentration change can be observed near GB at the depth of 1900 nm. As a result, thermal out diffusion of B along the GB can be excluded as a mechanism underlying the observed changes in GB composition under high temperature radiation.

Table 3. The lowest formation energy and the migration energy of defects in TiB_2 calculated from DFT. Here $V_{B/Ti}$ represent vacancies on the B/Ti sublattice, B/Ti_I represent B/Ti atoms in interstitial positions, B_I-V_{Ti} represents B interstitial and Ti vacancy complex, Ti_B corresponds to antisite defect, i.e., Ti_B is a Ti atom occupying B sublattice position.

Defects	**V_B**	**B_I**	**B_I-V_{Ti}**	**V_{Ti}**	**Ti_I**	**Ti_B**
Formation energy (eV)	2.78	6.00	6.11	4.35	12.62	9.93
Migration Energy (eV)	1.60	0.68	Immobile	6.13	0.52	Immobile

To rationalize the RIS observed in TiB_2, we analyzed the defect kinetics based on DFT calculations. We focused our analysis on point defects including FPs and anti-sites, because the formation of point defects is a direct consequence of irradiation. It is worth mentioning that when B interstitials encounter Ti vacancies, instead of forming B_{Ti} (E_f = 8.38 eV), they tend to form B_I-V_{Ti} complex (E_f = 6.11 eV) where B interstitial is attracted to the center of half octahedron formed by Ti vacancy and four B lattice atoms (Fig. S5). Analysis of defect migration energies can bring insights into which defects are mobile at the temperature of the experiments and therefore which defects are able to recombine with each other as well as migrate to GBs. We are not considering the migration of anti-sites or B_I-V_{Ti} complexes because they are immobile [56]. In this work, we consider only the most stable states of each defect type. Their formation energies and configurations are summarized in Table 3 and Fig. S5 (c and d), respectively.

In Table 3, the formation and migration energies are listed for the most stable defects in TiB_2. The tabulated values of migration energies correspond to a path with the lowest activation energy. The details of all possible migration paths are reported in Supplementary Materials (Fig. S6, Fig. S7, and Table S2). In the case of SiC, RIS was shown to be related to the presence of an energy barrier to recombination of C FPs [16]. In the case of TiB_2 the recombination processes for both Ti and B FPs are controlled by diffusion and do not have an additional barrier to defect recombination. Consequently, RIS in TiB_2 must be governed by a different mechanism.

As mentioned in Section 1, RIS observed in metallic alloys is typically driven by

variations in diffusivities among different species. However, we have found that this mechanism does not account for the observed B depletion in our experiments. As it is well known, the relationship between the diffusion coefficient of defects and the migration energy barrier is described by an Arrhenius equation, and a lower migration energy signifies a higher diffusivity. Based on the DFT calculations, summarized in Table 3, the Ti vacancy is immobile at the experimental temperature (600 ° C) due to the high migration energy barrier (6.13 eV). On the other hand, the B vacancy has a migration energy barrier of 1.60 eV, making it mobile but with a relatively lower diffusivity as compared to B and Ti interstitials. As for interstitials, with low migration energy barriers (0.52 eV for Ti and 0.68 eV for B), they exhibit comparable mobilities to interstitials in typical metals [57]. As diffusivities of interstitials are much higher than vacancies, interstitials can diffuse to the GB much faster. If interstitial migration was the only process relevant to RIS, at the end of the irradiation experiment, both Ti and B interstitials would pile up at the GB, resulting in an increase in elemental densities relative to the bulk density. However, as mentioned in Section 3.1, only Ti elemental density increased at the GB while B elemental density decreased at the GB, contradicting an explanation solely based on the different diffusivities of defects in TiB_2. Thus, there must exist another mechanism to explain the radiation-induced B depletion observed in TiB_2.

We found that the radiation-induced B depletion observed in our experiments can be understood by considering defect reactions involving antisites and B_I-V_{Ti} complexes as well the diffusivities of vacancies. In particular, antisites and B_I-V_{Ti}

complexes are immobile, and their impact on defect flux is found to occur through the preferential absorption or release of mobile defects via reactions. To further examine the effects of antisite and B_I-V_{Ti} complex, we explored the following reactions:

$$B_I + V_{Ti} \rightarrow B_I\text{-}V_{Ti} \text{ (-1.97 eV)} \quad (3)$$

$$Ti_I + V_B \rightarrow Ti_B \text{ (-5.47 eV)} \quad (4)$$

$$B_I\text{-}V_{Ti} + Ti_I \rightarrow Ti_{Ti} + B_I \text{ (-15.00 eV)} \quad (5)$$

$$Ti_B + B_I \rightarrow B_B + Ti_I \text{ (-3.31 eV)} \quad (6)$$

Here, the Ti_{Ti} corresponds to the Ti interstitials taking Ti sublattice positions and B_B corresponds to the B interstitials taking B sublattice positions. In this discussion, we focus exclusively on reactions involving interstitials due to their higher mobilities. The reaction energies for all reactions were provided alongside each reaction, based on DFT calculations of differences in defect formation energies. All four reactions bear negative energies, suggesting that they are energetically favorable, and are expected to take place in the material. Consequently, as FPs are produced, some fraction of them will be trapped as antisites and B_I-V_{Ti} complexes. Moreover, if antisites or B_I-V_{Ti} complexes encounter mobile interstitials, they can be converted to mobile defects. Furthermore, it is important to note that during the EDS line scans at different depths near the GB, no noticeable differences in local composition were observed. As depicted by SRIM profile (Fig. 2), samples exhibit different damage levels at distinct depths. Considering that the damage level varies by a factor of 4 between the minimum and maximum measured depths, the similarity in the extents of compositional change across different regions suggests that the GB composition

likely reached a steady state, where the defects with lower diffusivity dominate the defect diffusion. As the V_{Ti} is almost immobile, the diffusion of V_B to the GB becomes the dominant factor in this context. In addition, it is expected the V_{Ti} will have a high concentration in the grain interior. Consequently, the probability for reaction (3) in grain interior will be quite high. It is therefore not surprising that rate theory simulations show a substantial number of B_I trapped in the grain interior, forming B_I-V_{Ti} complex.

To further understand the impact of these reactions on segregation, we conducted separate rate theory simulations with either considering or excluding reactions involving antisites and B_I-V_{Ti} complexes. Both simulations accounted for FP recombination. When the contribution of reactions with antisites and B_I-V_{Ti} complexes to the elemental concentration was incorporated (Eqs. 3 – 6), the B concentration in the GB first increased and then decreased as time progressed (Fig. 5a). With the B concentration decreasing over time, a transition from B enrichment to B depletion can be observed at ~999 s (Fig. 5a). This means that B depletion would be observed on the experimental time scales of 18000 s. The significance of antisite defect reactions was confirmed by ignoring their contribution to elemental concentrations. In this scenario, the B concentration continued to increase with no trend reversal (Fig. 5b), which means that B enrichment would be observed at the end of the experiment. To summarize, our rate theory simulation confirmed the presence of B depletion in TiB_2 GBs and demonstrated that reactions involving antisites and B_I-V_{Ti} complexes played a significant role in the B depletion in TiB_2.

The rate theory model used here was first developed in previous work on SiC [16,57,58]. Detailed discussion of the rate theory model, including the boundary conditions used, can be found in Ref. [16] and in our Supplementary Materials. In the current analysis, carbon defects in the model were replaced by boron defects and the silicon defects were replaced by titanium defects. The formation and migration energies of defects were replaced correspondingly based on the current DFT calculation. In addition, based on our DFT calculations, the reactions (3) and (5) are barrierless. The diffusion pre-factors, activation energies of reactions (4) and (6), defect reaction radii and defect production ratios in TiB_2 are currently unknown and their study is beyond the scope of this work. Therefore, these parameters were taken to be the same as for SiC [16,59], since their values should be on the same order of magnitude for both SiC and TiB_2. Besides, these parameters were used only to qualitatively explain the trends in local composition. To understand the impact of defect production ratios on the defect flux, we varied the defect production ratios in our simulations from the case of no antisites produced to the case where all Ti interstitials and Ti vacancies transformed to Ti_B antisites and B_I-V_{Ti} complexes, respectively. For all conditions, we consistently observed a similar qualitative trend in B concentration profiles, characterized by an initial B enrichment followed by a subsequent decrease leading to B depletion. For each scenario, the onset time of the transition from B enrichment to B depletion was collected and summarized in Supplementary Materials (Table S3). The onset of the B depletion time showed some variations, with all of them falling within the time range of the current experiments

(18000 s). As the variation of defect production ratios has a negligible impact on the occurrence of B depletion, we chose to retain the ratios derived from SiC for our qualitative simulations shown in Fig. 5a and Fig. 5b, as they represent a set of physically plausible values based on molecular dynamics (MD) simulations [59].

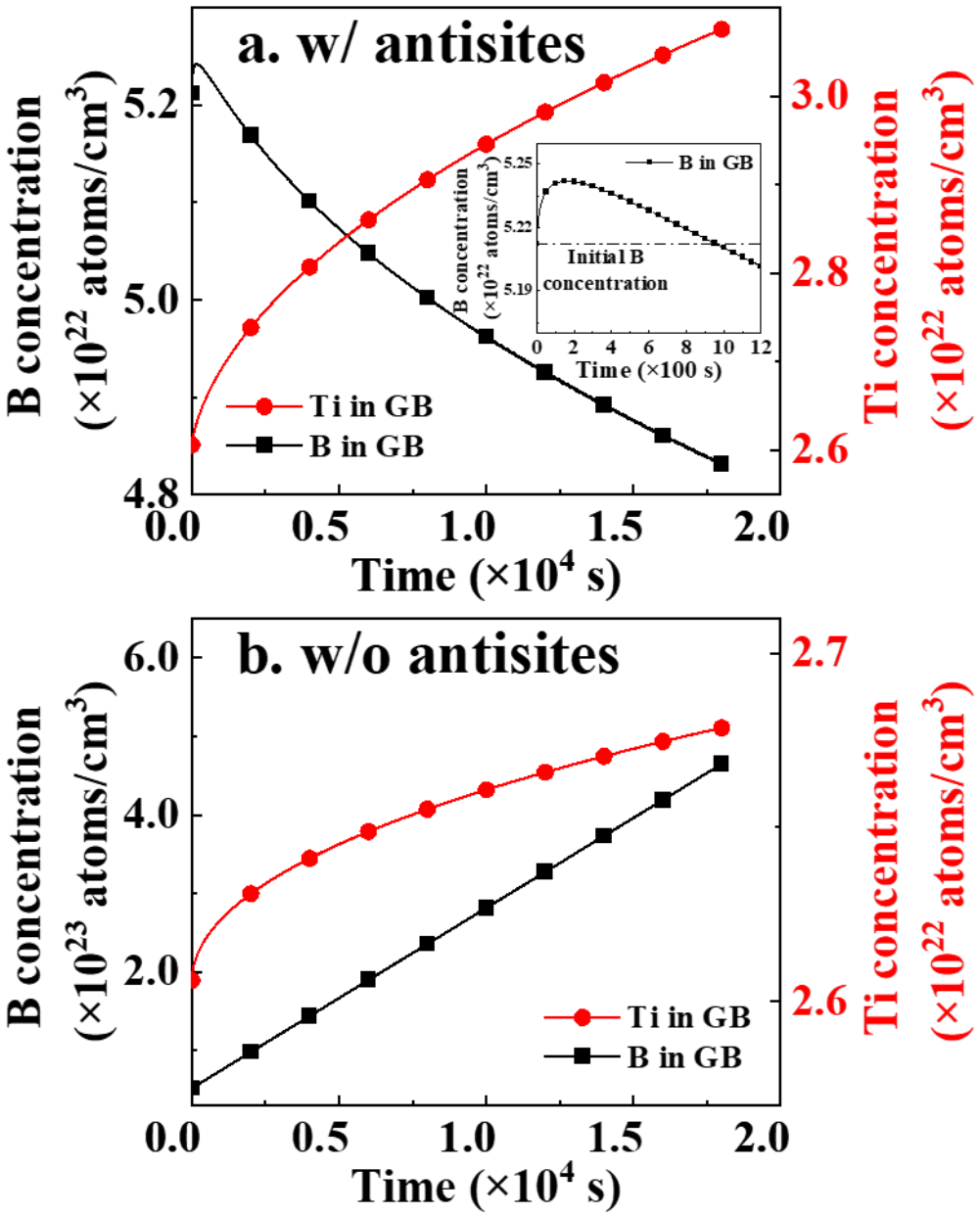

Figure 5. Results of rate theory calculations. Local concentration at the GB as a function of time with the defect production ratios the same as in SiC. (a) Reactions

involving antisites and B_I-V_{Ti} complexes were taken into consideration for the calculation of elemental concentration. The inset shows the local concentration of B as a function of time in the first 1200 s as the initial trend cannot be observed at the overall range. (b) Reactions involving antisites and B_I-V_{Ti} complexes were not taken into consideration while the FPs recombination was still considered for the calculation of elemental concentration. All concentrations were calculated by supposing defects diffused to the GB region cylinder shaped with a diameter of 500 nm and a length of 0.78 nm.

We also used the rate theory model to directly monitor concentrations of all the defects as a function of time, both in the bulk and at the GB to prove our hypothesis that vacancy mobilities can affect defect reactions and RIS. To calculate the concentration in the bulk, we considered all defects in the grain interior to be localized at the center of the grain in a region with the same size as the GB region. In the bulk region, the concentration of B_I-V_{Ti} increased with time and reached a much higher value than any other defects by the end of the simulation (Fig. 6a), which agrees with our expectation that immobile V_{Ti} serve as reaction sites for formation of B_I-V_{Ti} complexes and can trap a large number of B_I in grain interiors. We also found that the concentration of V_B at the GB was higher than that of B_I (Fig. 6b), consistent with a higher number of B interstitials being trapped on Ti vacancies. The larger number of V_B than B_I resulted in the occurrence of B depletion in GB. Moreover, as the V_B was confined to the B sublattice, for each V_B arriving at the GB, one B atom will be removed, further depleting the B atoms at the GB. In addition, when we

examined the initial few seconds of the simulation, we observed a lower concentration of V_B than B_I (Fig. 6d) in the GB, which agreed with the observation of a transition from B enrichment to B depletion over time (Fig. 4a). In summary, two mechanisms contributed to the observed B depletion. First, with the accumulation of V_{Ti} in grain interior due to its immobility, there exist a large number of reaction sites for the formation of B_I-V_{Ti} and consequently, many of the B_I defects are trapped in grain interior. The second mechanism is related to the diffusion of V_B to GB. As B_I concentration reaches a steady state in GB, the concentration of V_B in GB gradually increases with time and finally becomes higher than that of B_I with the arrival of V_B. In addition, as the V_B are confined to the B sublattice, the arrival of V_B will remove B atom from GB, which further depletes B at GB. These two mechanisms working together lead to depletion of B at the GB.

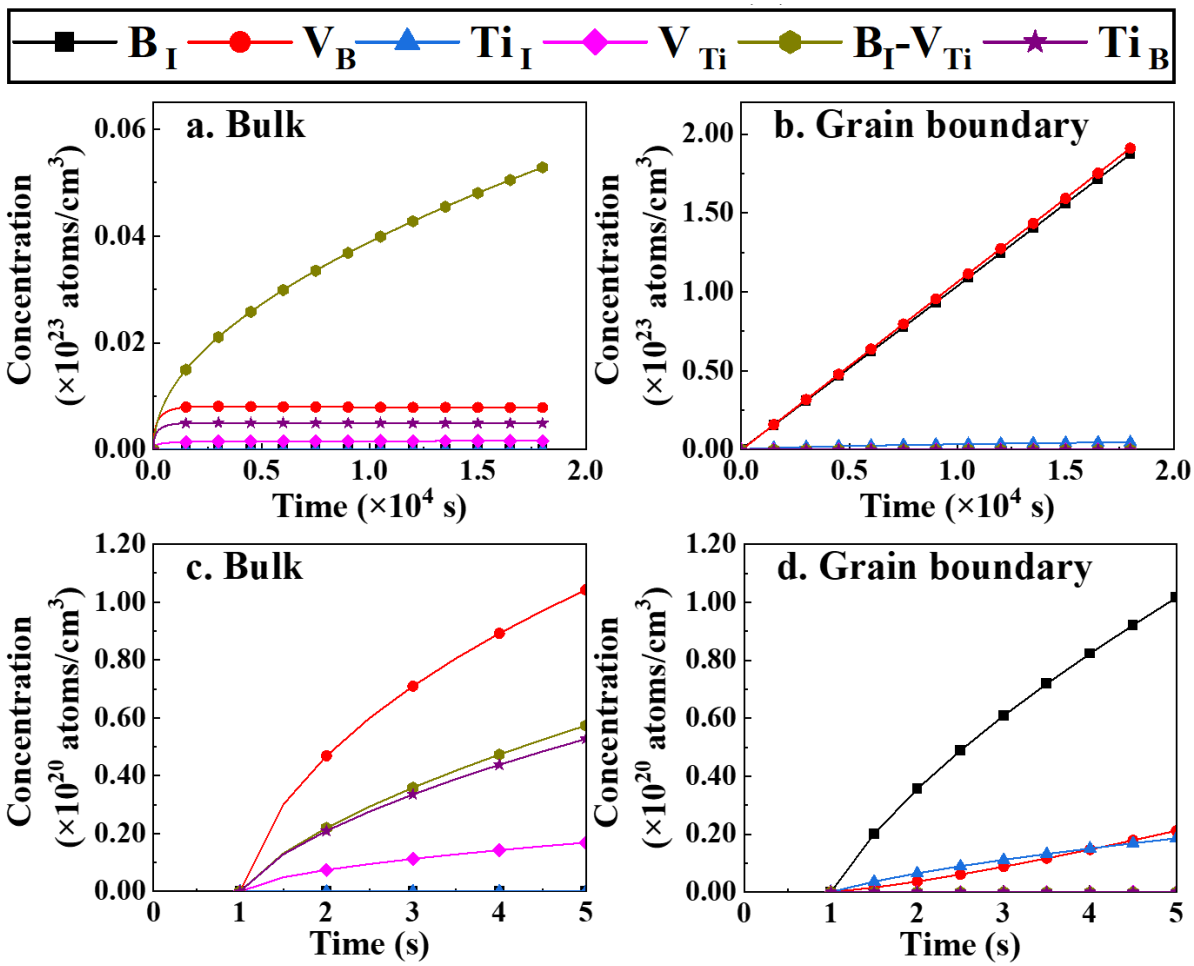

Figure 6. The defect concentrations according to the rate theory model (a) in the bulk and (b) in the GB regions. (c) and (d) are the zoomed-in images showing the first 5 seconds of the irradiation of (a) and (b), respectively. (a) and (c) The values of Ti_I and B_I are too small that they are hidden by the x-axis, (b) and (d) The values of V_{Ti}, B_I-V_{Ti} and Ti_B are too small that they are hidden by the x-axis.

3.3. Insights into temperature and dose dependence of RIS in TiB_2

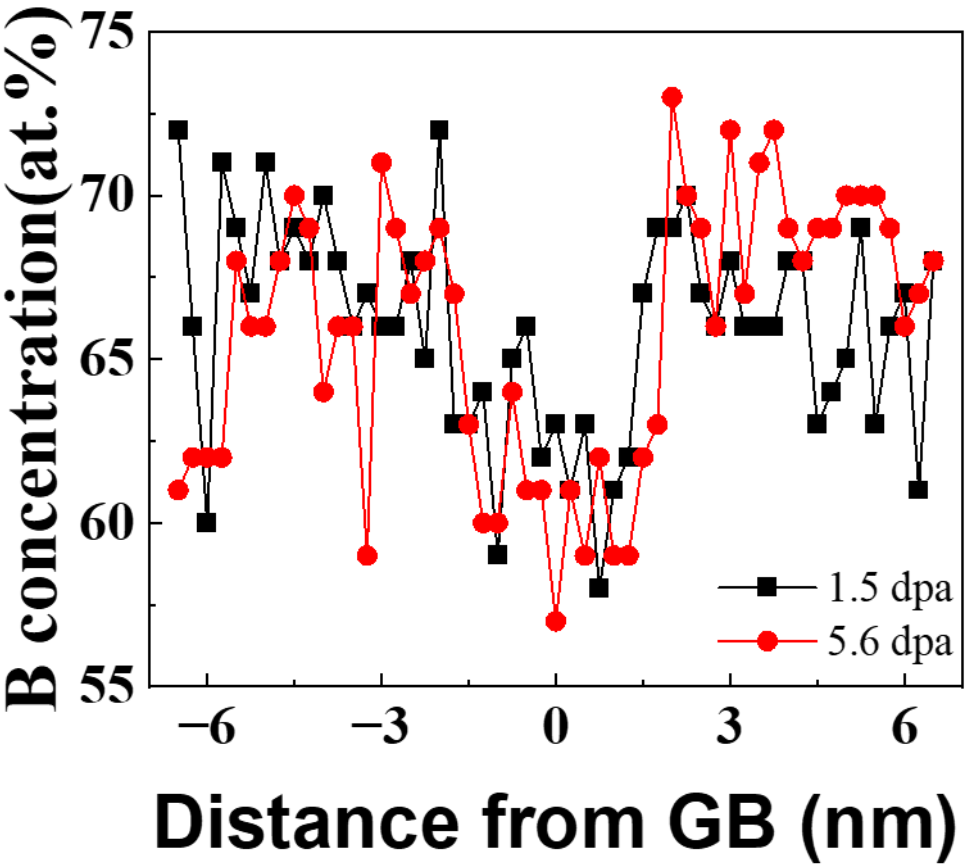

Figure 7. Local elemental compositions in TiB_2 irradiated at 600 °C to different damage levels along HAGB. Here, we pick the lowest damage level and the highest damage level as representatives.

In this work we focused primarily on providing evidence for the existence of RIS in TiB_2 and not on temperature- or dose-dependence of RIS. However, our data provides some interesting insights into these trends. For example, as we mentioned in Section 3.2, we did not notice much difference between EDS line scans near GB at different depths, which correspond to different damage doses (see SRIM profile in Fig. 2). The compositions as a function of distance from the GB measured at the minimum and maximum depths, which correspond to the lowest and highest damage levels, are shown in Fig. 7. As illustrated by Fig. 7, the local elemental compositions in TiB_2 irradiated at 600 °C to different damage levels overlap with each other. For this reason,

in Fig. 4 we have reported the averages in composition over the different line scans. However, the overlapping composition profiles in Fig. 7 suggest that it is possible that the compositions have reached a steady state and there is no dose dependence at these damage levels. Additional measurements of samples irradiated to different doses will be needed to confirm this phenomenon.

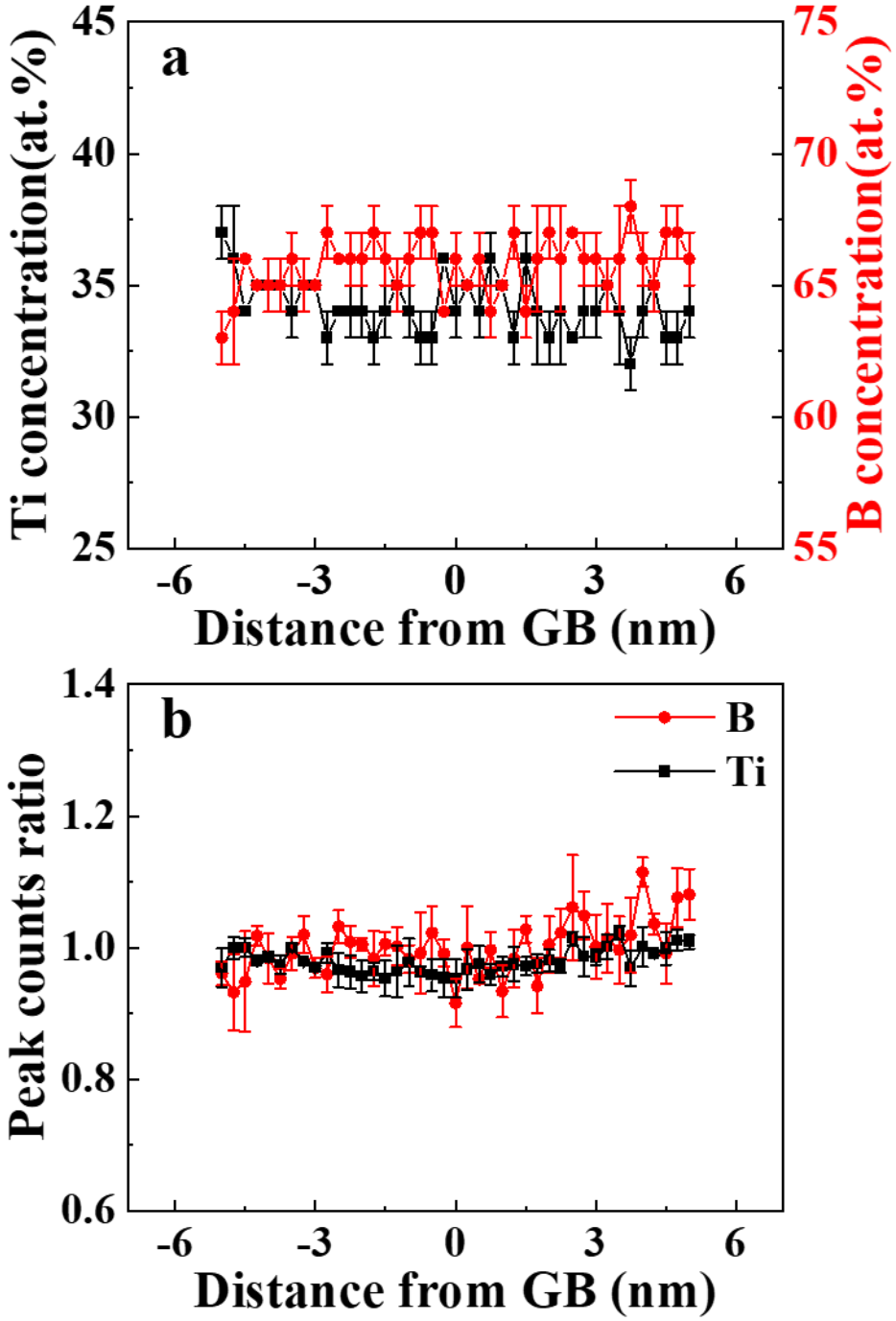

Figure 8. (a) Local elemental compositions in TiB_2 irradiated at 300 °C and (b) Typical peak count ratios near the damaged (irradiated) GB. The error bar corresponds to the standard deviation from the mean.

With respect to the temperature dependence of RIS, we have not explored the full range of temperatures, but we did analyze samples irradiated at 300°C. The results of our analysis of local composition as a function of distance from GB are shown in Fig. 8. We performed three line scans at different locations along a HAGB GB (misorientation angle of 74 °), ranging from a depth from 900 nm to 1700 nm. Average concentrations based on all measurements from the different line scans are plotted in Fig. 8a. The B concentration at GB was found to be 66 at.% and Ti concentration at GB was found to be 34 at.% (Fig. 8a). The composition near GB is very close to the bulk region, suggesting lack of RIS in TiB_2 when irradiated at 300 °C. The peak count ratios for both Ti and B measured at 300 °C also show no feature of RIS (Fig. 8b). These observations agree with our hypothesis that migration of V_B to the GB is crucial to RIS as V_B are immobile at 300 °C. Because V_B no longer diffuse to the GB, B depletion cannot be achieved at the GB, thus, there no longer exists RIS in TiB_2. In addition, the lack of RIS at 300 °C is consistent with the prediction of rate theory model simulations (Fig. S8). Finally, although in this work, we also studied the radiation damage in TiB_2 when irradiated at 150 °C, we did not characterize the composition change near the GB in this case because the sample was found to be porous, and we did not locate a GB good enough to study RIS.

4. Conclusions:

Our experiments revealed RIS in GBs of TiB_2 with modest Ti enrichment and significant B depletion. DFT calculations and rate theory modeling showed that RIS in TiB_2 is controlled by the formation of antisite defects via reactions between point defects. Specifically, for B, free B_I reacts with V_{Ti} and the product B_I-V_{Ti} complex is trapped in grain interior as it cannot diffuse, which is responsible for B depletion at the GBs. For Ti, there are two sources of Ti_I, one of which is from the displacement cascade and the other is the result of the antisite defect reactions. The Ti_I has a lower migration energy barrier than V_{Ti}, resulting in the modest Ti enrichment at the GBs. The mechanism of RIS in TiB_2 is distinct from what was previously found in metals and other ceramics. The observation of RIS in TiB_2 further suggests that RIS can be widespread in ceramics even when they form line compounds. Our joint experimental and computational study provides a new understanding of how the complex energy landscape in ceramics can affect the defects kinetics and the mechanisms of the RIS.

Acknowledgment

The authors gratefully acknowledge support from the Department of Energy Basic Energy Science Program (grant # DEFG02–08ER46493).

Declaration of Generative AI and AI-assisted technologies in the writing process

During the preparation of this work, the authors used ChatGPT in order to improve the language. After using this tool/service, the authors reviewed and edited the content as needed and took full responsibility for the content of the publication.

References

[1] F. Granberg, K. Nordlund, M.W. Ullah, K. Jin, C. Lu, H. Bei, L.M. Wang, F. Djurabekova, W.J. Weber, Y. Zhang, Mechanism of Radiation Damage Reduction in Equiatomic Multicomponent Single Phase Alloys, Phys. Rev. Lett. 116 (2016) 135504.

[2] G.S. Was, Fundamentals of radiation materials science: metals and alloys, springer, 2016.

[3] X. Zhang, K. Hattar, Y. Chen, L. Shao, J. Li, C. Sun, K. Yu, N. Li, M.L. Taheri, H. Wang, J. Wang, M. Nastasi, Radiation damage in nanostructured materials, Prog. Mater. Sci. 96 (2018) 217–321.

[4] R.S. BARNES, Embrittlement of Stainless Steels and Nickel-Based Alloys at High Temperature Induced by Neutron Radiation, Nature. 206 (1965) 1307–1310.

[5] J.Y. Kim, H. Zhang, R. Su, J. Xi, S. Wei, P. Richardson, L. Liu, E. Kisi, J.H. Perepezko, I. Szlufarska, Defect recovery processes in Cr-B binary and Cr-Al-B MAB phases: structure-dependent radiation tolerance, Acta Mater. 235 (2022) 118099.

[6] Z. Jiao, G.S. Was, Novel features of radiation-induced segregation and radiation-induced precipitation in austenitic stainless steels, Acta Mater. 59 (2011) 1220–1238.

[7] M.-R. He, S. Wang, S. Shi, K. Jin, H. Bei, K. Yasuda, S. Matsumura, K. Higashida, I.M. Robertson, Mechanisms of radiation-induced segregation in CrFeCoNi-based single-phase concentrated solid solution alloys, Acta Mater. 126 (2017) 182–193.

[8] J.P. Wharry, G.S. Was, The mechanism of radiation-induced segregation in ferritic–martensitic alloys, Acta Mater. 65 (2014) 42–55.

[9] T.R. Allen, J.I. Cole, J. Gan, G.S. Was, R. Dropek, E.A. Kenik, Swelling and radiation-induced segregation in austentic alloys, J. Nucl. Mater. 342 (2005) 90–100.

[10] A. Etienne, B. Radiguet, N.J. Cunningham, G.R. Odette, P. Pareige, Atomic scale investigation of radiation-induced segregation in austenitic stainless steels, J. Nucl. Mater. 406 (2010) 244–250.

[11] K.G. Field, L.M. Barnard, C.M. Parish, J.T. Busby, D. Morgan, T.R. Allen, Dependence on grain boundary structure of radiation induced segregation in a 9wt.% Cr model ferritic/martensitic steel, J. Nucl. Mater. 435 (2013) 172–180.

[12] L.E. Rehn, P.R. Okamoto, H. Wiedersich, Dose dependence of radiation-induced segregation in Ni-1 at% Si, J. Nucl. Mater. 80 (1979) 172–179.

[13] S.M. Bruemmer, E.P. Simonen, P.M. Scott, P.L. Andresen, G.S. Was, J.L.

Nelson, Radiation-induced material changes and susceptibility to intergranular failure of light-water-reactor core internals, J. Nucl. Mater. 274 (1999) 299–314.

[14] J.T. Busby, G.S. Was, E.A. Kenik, Isolating the effect of radiation-induced segregation in irradiation-assisted stress corrosion cracking of austenitic stainless steels, J. Nucl. Mater. 302 (2002) 20–40.

[15] S.M. Bruemmer, G.S. Was, Microstructural and microchemical mechanisms controlling intergranular stress corrosion cracking in light-water-reactor systems, J. Nucl. Mater. 216 (1994) 348–363.

[16] X. Wang, H. Zhang, T. Baba, H. Jiang, C. Liu, Y. Guan, O. Elleuch, T. Kuech, D. Morgan, J.-C. Idrobo, P.M. Voyles, I. Szlufarska, Radiation-induced segregation in a ceramic, Nat. Mater. 19 (2020) 992–998.

[17] J. Xi, H. Zhang, R. Su, S. Wei, B. Queylat, T. Kim, A. Couet, I. Szlufarska, Coupling of radiation and grain boundary corrosion in a ceramic, Submitted. (2023).

[18] J. Xi, I. Szlufarska, Control of Surface Chemical Reactions through Solid Stiffness, Phys. Rev. Lett. 129 (2022) 106101.

[19] J. Xi, C. Liu, I. Szlufarska, Effects of point defects on oxidation of 3C–SiC, J. Nucl. Mater. 538 (2020) 152308.

[20] M.A. Tunes, F.C. da Silva, O. Camara, C.G. Schön, J.C. Sagás, L.C. Fontana, S.E. Donnelly, G. Greaves, P.D. Edmondson, Energetic particle irradiation study of TiN coatings: are these films appropriate for accident tolerant fuels?, J.

Nucl. Mater. 512 (2018) 239–245.

[21] M.A. Tunes, M. Imtyazuddin, C. Kainz, S. Pogatscher, V.M. Vishnyakov, Deviating from the pure MAX phase concept: Radiation-tolerant nanostructured dual-phase Cr2AlC, Sci. Adv. 7 (2021) 1–13.

[22] T. Velikanova and Mikhail Turchanin, M. Materials Science International Team, B-Mo-Ti Ternary Phase Diagram Evaluation · Phase diagrams, crystallographic and thermodynamic data: Datasheet from MSI Eureka in SpringerMaterials (https://materials.springer.com/msi/docs/sm_msi_r_10_013136_01).

[23] W.E. Lee, E. Giorgi, R. Harrison, A. Maître, O. Rapaud, Nuclear Applications for Ultra-High Temperature Ceramics and MAX Phases, in: Ultra-High Temp. Ceram., John Wiley & Sons, Inc, Hoboken, NJ, 2014: pp. 391–415.

[24] R.G. Munro, Material properties of titanium diboride, J. Res. Natl. Inst. Stand. Technol. 105 (2000) 709.

[25] A. Agarwal, N.B. Dahotre, Comparative wear in titanium diboride coatings on steel using high energy density processes, Wear. 240 (2000) 144–151.

[26] C. Subramanian, T.S.R.C. Murthy, A.K. Suri, Synthesis and consolidation of titanium diboride, Int. J. Refract. Met. Hard Mater. 25 (2007) 345–350.

[27] L.-H. Li, H.-E. Kim, E. Son Kang, Sintering and mechanical properties of titanium diboride with aluminum nitride as a sintering aid, J. Eur. Ceram. Soc. 22 (2002) 973–977.

[28] H.R. Baumgartner, R.A. Steiger, Sintering and Properties of Titanium Diboride

Made from Powder Synthesized in a Plasma-Arc Heater, J. Am. Ceram. Soc. 67 (2006) 207–212.

[29] S.H. Kang, D.J. Kim, E.S. Kang, S.S. Baek, Pressureless Sintering and Properties of Titanium Diboride Ceramics Containing Chromium and Iron, J. Am. Ceram. Soc. 84 (2001) 893–895.

[30] G.B. Raju, B. Basu, Densification, sintering reactions, and properties of titanium diboride with titanium disilicide as a sintering aid, J. Am. Ceram. Soc. 90 (2007) 3415–3423.

[31] P.H. Mayrhofer, C. Mitterer, J.G. Wen, J.E. Greene, I. Petrov, Self-organized nanocolumnar structure in superhard TiB2 thin films, Appl. Phys. Lett. 86 (2005) 131909.

[32] H.O. Pierson, E. Randich, Titanium diboride coatings and their interaction with the substrates, Thin Solid Films. 54 (1978) 119–128.

[33] M. Kaminsky, S.K. Das, Surface damage of TiB2 and C coatings under energetic D+ AND 4He+ irradiations, J. Nucl. Mater. 85–86 (1979) 1095–1100.

[34] S.K. Das, M. Kaminsky, Deuterium and helium ion irradiation effects on TiB2 coatings, Thin Solid Films. 63 (1979) 269–275.

[35] E.U. Grinik, V.V. Ogorodnikov, A.G. Krainy, Fracturing of borides under neutron irradiation, J. Nucl. Mater. 233–237 (1996) 1349–1354.

[36] T. Koyanagi, Y. Katoh, C. Ang, D. King, G.E. Hilmas, W.G. Fahrenholtz, Response of isotopically tailored titanium diboride to neutron irradiation, J. Am.

Ceram. Soc. 102 (2019) 85–89.

[37] R. Lokesh, P. Bellon, R.S. Averback, Nanostructuring of Cu–TiB2 induced by ion irradiation, J. Nucl. Mater. 423 (2012) 9–15.

[38] A. Bhattacharya, C.M. Parish, T. Koyanagi, C.M. Petrie, D. King, G. Hilmas, W.G. Fahrenholtz, S.J. Zinkle, Y. Katoh, Nano-scale microstructure damage by neutron irradiations in a novel Boron-11 enriched TiB2 ultra-high temperature ceramic, Acta Mater. 165 (2019) 26–39.

[39] S. Madtha, C. Lee, K.S. Ravi Chandran, Physical and Mechanical Properties of Nanostructured Titanium Boride (TiB) Ceramic, J. Am. Ceram. Soc. 91 (2008) 1319–1321.

[40] L. Liu, C. Sun, C. Zhang, P.M. Voyles, J. Fournelle, A. Handt, J.H. Perepezko, Examination of B in the Mo solid solution (Moss) in Moss + Mo5SiB2 + Mo2B alloys, Scr. Mater. 163 (2019) 62–65.

[41] R.E. Stoller, M.B. Toloczko, G.S. Was, A.G. Certain, S. Dwaraknath, F.A. Garner, On the use of SRIM for computing radiation damage exposure, Nucl. Instruments Methods Phys. Res. Sect. B Beam Interact. with Mater. Atoms. 310 (2013) 75–80.

[42] G. Kresse, J. Furthmüller, Efficient iterative schemes for ab initio total-energy calculations using a plane-wave basis set, Phys. Rev. B. 54 (1996) 11169–11186.

[43] G. Kresse, D. Joubert, From ultrasoft pseudopotentials to the projector augmented-wave method, Phys. Rev. B. 59 (1999) 1758–1775.

[44] J.P. Perdew, K. Burke, M. Ernzerhof, Generalized Gradient Approximation Made Simple, Phys. Rev. Lett. 77 (1996) 3865–3868.

[45] H.J. Monkhorst, J.D. Pack, Special points for Brillouin-zone integrations, Phys. Rev. B. 13 (1976) 5188–5192.

[46] J.Y. Kim, J. Xi, H. Zhang, I. Szlufarska, Defect chemistry of Cr-B binary and Cr-Al-B MAB phases: Effects of covalently bonded B networks, Phys. Rev. Mater. 5 (2021) 113603.

[47] G. Henkelman, B.P. Uberuaga, H. Jónsson, A climbing image nudged elastic band method for finding saddle points and minimum energy paths, J. Chem. Phys. 113 (2000) 9901–9904.

[48] Y. Tajima, W.D. Kingery, Grain-boundary segregation in aluminium-doped silicon carbide, J. Mater. Sci. 17 (1982) 2289–2297.

[49] P. Wynblatt, G.S. Rohrer, F. Papillon, Grain boundary segregation in oxide ceramics, J. Eur. Ceram. Soc. 23 (2003) 2841–2848.

[50] S.B. Desu, D.A. Payne, Interfacial Segregation in Perovskites: II, Experimental Evidence, J. Am. Ceram. Soc. 73 (1990) 3398–3406.

[51] C.J. Marvel, K.D. Behler, J.C. LaSalvia, R.A. Haber, M.P. Harmer, Grain boundary segregation in Si-doped B-based ceramics and its effect on grain boundary cohesion, Acta Mater. 227 (2022) 117684.

[52] W. Böcker, H. Landfermann, H. Hausner, Sintering of alpha silicon carbide with additions of aluminium, POWDER Metall. Int. 11 (1979) 83–85.

[53] J. Emmerlich, D. Music, P. Eklund, O. Wilhelmsson, U. Jansson, J.M.

Schneider, H. Högberg, L. Hultman, Thermal stability of Ti3SiC2 thin films, Acta Mater. 55 (2007) 1479–1488.

[54] T. El-Raghy, M.W. Barsoum, Diffusion kinetics of the carburization and silicidation of Ti3SiC2, J. Appl. Phys. 83 (1998) 112–119.

[55] W.D. Callister Jr, Materials science and engineering an introduction, 2007.

[56] H. Zhang, J.Y. Kim, R. Su, P. Richardson, J. Xi, E. Kisi, J. O'Connor, L. Shi, I. Szlufarska, Defect behavior and radiation tolerance of MAB phases (MoAlB and Fe2AlB2) with comparison to MAX phases, Acta Mater. 196 (2020) 505–515.

[57] N. Swaminathan, D. Morgan, I. Szlufarska, Role of recombination kinetics and grain size in radiation-induced amorphization, Phys. Rev. B. 86 (2012) 214110.

[58] N. Swaminathan, D. Morgan, I. Szlufarska, Ab initio based rate theory model of radiation induced amorphization in β-SiC, J. Nucl. Mater. 414 (2011) 431–439.

[59] N. Swaminathan, P.J. Kamenski, D. Morgan, I. Szlufarska, Effects of grain size and grain boundaries on defect production in nanocrystalline 3C–SiC, Acta Mater. 58 (2010) 2843–2853.

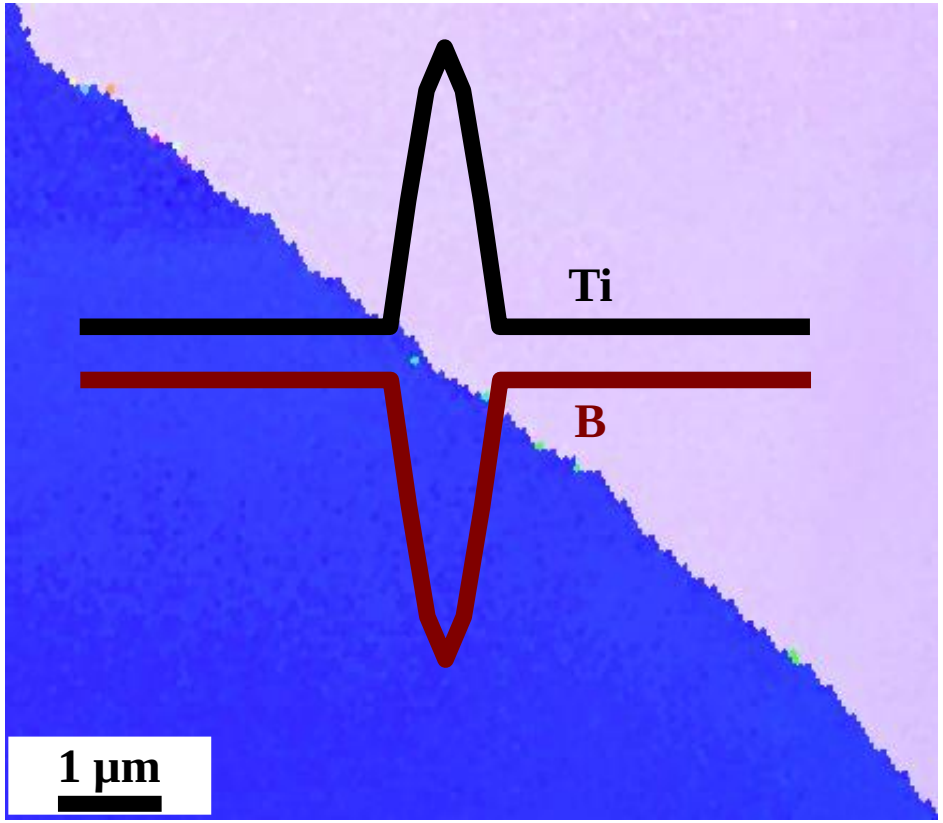
Ti
B
1 µm